PCCP

PAPER

View Article Online
View Journal | View Issue

Open Access Article. Published on 05 June 2025. Downloaded on 3/3/2026 10:40:12 AM.
This article is licensed under a Creative Commons Attribution-NonCommercial 3.0 Unported Licence.

Check for updates

Cite this: *Phys. Chem. Chem. Phys.*, 2025, **27**, 13464

Effect of rare earth size on network structure and glass forming ability in binary aluminum garnets†

Stephen K. Wilke, *[ab] Chris J. Benmore, [b] Randall E. Youngman, [c] Benjamin J. A. Moulton, [d] Abdulrahman Al-Rubkhi[a] and Richard Weber [ab]

Received 16th April 2025,
Accepted 4th June 2025

DOI: 10.1039/d5cp01467k

rsc.li/pccp

Rare earth aluminate glasses are potentially useful for optical, luminescence, and laser applications. As reluctant glass formers, these materials exhibit unconventional atomic structures. To better understand how their structures correlate with glass formation, we investigate two rare earth aluminum garnet melts, $La_3Al_5O_{12}$ (LAG) and $Yb_3Al_5O_{12}$ (YbAG), which represent the relative extremes of good and poor glass forming ability in rare earth aluminates. Structural models have been refined to high-energy X-ray diffraction data over 1340–2740 K. Both melts contain mixtures of AlO_4, AlO_5, and AlO_6 polyhedra, with larger fractions of $^{[5]}$Al and $^{[6]}$Al in YbAG. Extrapolation of the Al–O coordination distributions to the glass transition match closely with ^{27}Al nuclear magnetic resonance measurements of $(La_{1-z}Y_z)_3Al_5O_{12}$ glasses, z = 0 to 1. During cooling, the mean coordination numbers increase for La–O in LAG from 6.45(8) to 6.98(8) and for Yb–O in YbAG from 6.02(8) to 6.21(8). Linkedness among Al–O polyhedra at ~2450 K is mostly corner-sharing, with 9% edge-sharing in LAG and 19% in YbAG. Among $^{[4]}$Al units, both melts have 6% edge-sharing that convert to all corner-sharing upon cooling. Network connectivity is compared using a newly defined metric, K^n, that is similar to the Q^n distribution but that accounts for the edge-sharing and triply bonded oxygen present in these melts. The lower glass forming ability in YbAG as compared to LAG correlates with more edge-sharing, associated with the larger fractions of $^{[5]}$Al and $^{[6]}$Al, and lower connectivity among $^{[4]}$Al units.

1. Introduction

Rare earth aluminum garnets, $R_3Al_5O_{12}$, are important materials in a variety of optical applications[1–6] – laser gain media, phosphors, and Faraday isolators – and as thermal barrier coatings.[7,8] Although most applications currently use the crystalline form, these compositions can be vitrified using containerless processes such as levitation melting.[9,10] The use of levitation avoids container-induced crystal nucleation and avoids contaminating reactions with crucible materials at the very high temperatures required for melting, typically above 2200 K.[11] This approach has recently been used to study phase transformations and thermal expansion in high-entropy rare earth sesquioxides.[12] Although reluctant to vitrify, binary aluminum garnet compositions can be processed into glass for the rare earth sesquioxides from La through Ho. Glass forming ability worsens as the rare earth size decreases, and crystal-free glass has not been reported for Er, Tm, Yb, or Lu.[13] Given the potential of rare earth aluminates for functional glass applications,[2,10,14] it is useful to establish correlations between the glass forming ability and atomic structure across the rare earth series.

A thorough structural analysis of Al_2O_3–La_2O_3 and Al_2O_3–Y_2O_3 glass binaries, including the garnet compositions $La_3Al_5O_{12}$ (LAG) and $Y_3Al_5O_{12}$ (YAG), was recently published by Watanabe *et al.*[15] that details differences in the Al–O atomic network and how those changes are linked to the rare earth modifier cations. La and Y are a useful pair for comparison because they fall at the extremes of rare earth aluminum garnet glass formation: La^{3+} being the largest rare earth cation (radius of 1.032 Å for 6-fold coordination[16]), and Y^{3+} (0.9 Å) being the smallest for which crystal-free glass has been reported.[13] Their study showed that the atomic networks in LAG and YAG comprise mixtures of AlO_4, AlO_5, and AlO_6 polyhedra ($^{[4]}$Al, $^{[5]}$Al, $^{[6]}$Al) connected mostly in corner-sharing arrangements. The Al–O coordination distributions were 91% $^{[4]}$Al, 8% $^{[5]}$Al, and 1% $^{[6]}$Al in LAG and 61, 28, 11% in YAG.

Watanabe *et al.*[15] also presented a model that describes the Al–O network for varying modifier content in the binaries based

[a] *Materials Development, Inc., Arlington Heights, IL 60004, USA. E-mail: swilke@matsdev.com*
[b] *X-ray Science Division, Advanced Photon Source, Argonne National Laboratory, Lemont, IL 60439, USA*
[c] *Science and Technology Division, Corning Incorporated, Corning, NY 14831, USA*
[d] *Inamori School of Engineering at the New York State College of Ceramics, Alfred University, Alfred, NY 14802, USA*

† Electronic supplementary information (ESI) available. See DOI: https://doi.org/10.1039/d5cp01467k

 This journal is © the Owner Societies 2025

Open Access Article. Published on 05 June 2025. Downloaded on 3/3/2026 10:40:12 AM.
This article is licensed under a Creative Commons Attribution-NonCommercial 3.0 Unported Licence.

on the [O]/[Al] ratio, using charge balance and assuming no triply bonded oxygen. When [O]/[Al] = 2, all Al can exist as corner-sharing AlO_4 (*i.e.*, a Q^4 network) and be fully charge-compensated by modifier cations. Compositions richer in modifier content have [O]/[Al] > 2 and will be partially depolymerized, as the excess modifier creates nonbridging oxygen. (For the garnet composition, [O]/[Al] = 2.4.) This model matches the reported structure for a variety of alkaline earth modified aluminate glasses, which contain essentially 100% AlO_4 for [O]/[Al] ≥ 2.[17–19] For Al_2O_3–R_2O_3 glasses, however, a mixture of Al–O coordination environments is present even for [O]/[Al] = 2. The presence of higher-coordinated $^{[5]}$Al and $^{[6]}$Al indicates that some modifiers are playing a different role in the glass structure than charge-compensating the $^{[4]}$Al network, and the structural complexity is not captured by the assumptions of all corner-sharing and no triply bonded oxygen.[15]

In this study, we continue the investigation of glass formation and atomic structure in rare earth aluminates, specifically of the garnet composition. First, we compare the structural changes in melts of LAG and $Yb_3Al_5O_{12}$ (YbAG) during cooling using high-energy X-ray diffraction. YbAG was selected because it is the largest rare earth (0.868 Å) that does not form crystal-free glass for any composition in the Al_2O_3–Yb_2O_3 binary.[13] Second, we examine the changes in Al–O coordination distributions across the ternary compositional series of glasses $(La_{1-z}Y_z)_3Al_5O_{12}$, z = 0 to 1, using ^{27}Al magic angle spinning nuclear magnetic resonance spectroscopy (MAS NMR). By comparing the glass and melt structures, network changes during melt quenching can be correlated with the relative glass forming abilities for LAG and YbAG.

2. Experimental methods

Polycrystalline samples of LAG and YbAG were prepared from the unary oxides (≥99.9% purity) by mechanical mixing and laser beam heating to form spheroids *ca.* 2.5 mm in diameter. High-energy X-ray diffraction measurements were collected for these samples in the molten and supercooled liquid states using aerodynamic levitation and laser beam heating, according to previously described methods.[20,21] Pyrometric temperature measurement uncertainty was ±30 K.[22] The diffraction of 100.04 keV X-rays was measured in transmission geometry using an area detector. Data reduction followed established procedures[23–25] to obtain the X-ray weighted total structure factors, $S(Q)$, for LAG melts ranging from 1340–2740 K, where $Q = 4\pi \sin\theta/\lambda$ is the momentum transfer, 2θ is the scattering angle, and λ is the X-ray wavelength. Real-space pair distributions functions (PDFs) were obtained by the sine Fourier transform of the structure factors, using Q_{max} = 20.5 Å^{-1} and no Lorch modification function. Analogous measurements on YbAG over 1770–2630 K were recently reported.[22]

Structural models for molten LAG were obtained from empirical potential structure refinements (EPSR) of the X-ray structure factors at 1340, 1720, 2060, 2420, and 2740 K. EPSR is a reverse Monte Carlo based simulation technique, in which simple, pre-defined interatomic potentials are refined by comparing the simulated and experimental scattering to bring the former into agreement with the latter.[26] The simulation procedure follows the details previously reported,[22] using the initial potential parameters listed in Table S1 of the ESI.† Melt densities were assumed to be 4.46 to 4.32 g cm^{-3}, equivalently 0.07228 to 0.06992 atoms Å^{-3}, for 1340 to 2740 K. These are ∼3% lower than the density reported for LAG glass, 4.53 g cm^{-3} (ref. 15) and were chosen to have a thermal expansion similar to the measured value for molten YbAG.[22]

Coordination number distributions for Al–O, R–O (R = La or Yb), and O–Al atom pairs were calculated in EPSR and averaged over 10 000 configurations. Cutoff distances were set to correspond to the minimum after the first peak in each partial PDF: 2.35 Å for Al–O and 3.25 Å for La–O in LAG, and 2.61 Å for Al–O and 3.01 Å for Yb–O in YbAG (Fig. S1, ESI†). For network linkedness analyses, the number of corner-, edge-, and face-sharing connections between Al–O polyhedra were counted on the basis of 1, 2, or 3 shared oxygen between neighboring polyhedra. For oxygen participating in the Al–O network, the fractions of nonbridging, bridging, and triply bonded oxygen were calculated based on their connection to 1, 2, or 3 Al–O polyhedra. This analysis of the oxygen fractions was performed twice: first, while defining the network to comprise only AlO_4 units, and then again while defining the network to comprise AlO_4 and AlO_5 units. For connectivity analyses, a modification of the conventional Q^n distribution was calculated to account for the presence of higher-coordinated Al–O polyhedra, edge-sharing, and triply bonded oxygen. A full explanation is given in Section 3.2 in the context of the results. These network linkedness and connectivity calculations were averaged over 100 configurations sampled evenly over the 10 000 EPSR iterations used for coordination number distributions.

For comparison, the coordination distributions of Al–O were measured on LAG and YAG glasses using ^{27}Al MAS NMR. In order to avoid issues with the paramagnetic properties of Yb^{3+}, YAG was measured in lieu of YbAG. This choice was also largely driven by their similar cation sizes and since the latter glass cannot be obtained without some crystalline fraction. Although Yb can occur in the 2+ oxidation state, unlike Y, only Yb^{3+} is expected in these aluminates given the oxidizing conditions and that even intentional preparation of Yb^{2+} materials is challenging and requires highly reducing conditions.[27,28]

^{27}Al MAS NMR measurements were collected on glasses of $(La_{1-z}Y_z)_3Al_5O_{12}$, z = 0 to 1, at 16.4 T (182.34 MHz resonance frequency) using an Agilent DD2 spectrometer, an Agilent triple resonance 3.2 mm MAS NMR probe, and a 700/54 Premium Shielded Magnet. Glasses were loaded into low-Al content zirconia rotors with an outer diameter of 3.2 mm. Single pulse experiments were performed with a 0.6 μs radio-frequency pulse width (π/12 tip angle), a 5 s recycle delay between scans, and signal averaging of nominally 800 scans. The sample spinning frequency was computer controlled to 20.0 kHz. The signal processing was performed without added line broadening, using commercial software (Agilent VnmrJ). The spectral fitting was performed in DMFit[29] making use of the Czjzek

Open Access Article. Published on 05 June 2025. Downloaded on 3/3/2026 10:40:12 AM.
This article is licensed under a Creative Commons Attribution-NonCommercial 3.0 Unported Licence.

function to reproduce second-order quadrupolar line shapes for the different Al coordination environments, yielding fractions of [4]Al, [5]Al, and [6]Al (Fig. S2, ESI†). The ^{27}Al shift was referenced to an external aqueous solution of aluminum nitrate at 0.0 ppm.

^{27}Al triple-quantum magic-angle spinning (3QMAS) NMR data were collected at 16.4 T using a hypercomplex 3QMAS pulse sequence with a Z filter.[30] The solid 3π/2 and π/2 pulse widths were optimized to 3.0 and 1.1 μs, respectively. A lower power π/2 pulse width of 15 μs was used as the soft reading pulse of the Z filter, following a storage period of 50 μs (one rotor cycle). The ^{27}Al 3QMAS NMR spectra were typically measured using 120 to 960 acquisitions at each of 64 to 100 t_1 points, with a recycle delay of 1 s. The datasets were Fourier-transformed and phase-corrected (sheared) using commercial software (VnmrJ), without additional apodization.

3. Results and discussion

The LAG X-ray structure factors are shown in Fig. 1(a). As temperature increases, the first principal peak in $S(Q)$ *ca.* 2.02 Å^{-1} shifts to lower Q, consistent with bulk thermal expansion in the melt (Fig. 1(a), inset). In the differential PDFs, Fig. 1(b), the first two peaks attributable to Al–O *ca.* 1.73 Å and La–O *ca.* 2.42 Å are clearly distinguished. All peaks in the PDFs broaden with increasing temperature due to thermal disordering, as was observed for YbAG.[22] Interestingly, the first coordination shell for La–O shifts slightly to shorter distances (2.38 Å) at higher temperatures, while the Al–O peak position remains constant (Fig. 1(b), inset). The slope of $D(r)$ at low-r is consistent with the expected value of $-4\pi\rho$, with ρ = 0.07228 to 0.06992 atoms Å^{-3} for 1340 to 2740 K.

The X-ray weighted atomic partial pair correlations from EPSR for molten LAG at 2420 K are shown in Fig. 1(c), along with the total PDFs from EPSR and the X-ray measurement. The broad La–O first peak is indicative of a wide distribution of coordination environments. The model is in good agreement with the experiment, though the model exhibits a clearer separation of the Al–O and La–O first coordination shells. Using the partials from EPSR, detailed analyses of the coordination environments and network structure can be made.

3.1. Cation–oxygen coordination

Coordination number distributions for Al–O and La–O were calculated from EPSR at each modeled temperature. To understand the structural changes that happen during melt quenching, we will begin with the melt and proceed through cooling, *i.e.*, moving right-to-left in each panel of Fig. 2. Beginning with the melt at 2740 K, LAG contains mainly [4]Al, 83%, with 8% each of [3]Al and [5]Al, and 1% [6]Al (Fig. 2(a)). The presence of [3]Al is consistent with numerous structural models – from reverse Monte Carlo and molecular dynamics approaches – that have been published for molten and amorphous Al_2O_3,[31] though direct experimental measurements have not been reported. As the melt is supercooled (T_m = 2275 K[11]), the fraction of [4]Al grows to 92% at the expense of [3]Al, while [5]Al and [6]Al decrease slightly. The distribution obtained from ^{27}Al MAS NMR on the glasses was 90% [4]Al, 9% [5]Al, and 1% [6]Al, shown in Fig. 2(a) at T_g = 1118 K[13] on the assumption that no significant coordination changes occur below the glass transition. These glass values agree within 2% with the extrapolated temperature trend of the EPSR models and with the study by Watanabe *et al.*[15] The mean Al–O coordination increases during cooling from 4.01 in the melt to 4.11 in the glass.

High-energy X-ray diffraction of molten YbAG was recently published.[22] Compared to LAG, molten YbAG[22] at 2630 K contains a greater mixture of Al–O coordination environments, as shown in Fig. 3(a): 54% [4]Al, 36% [5]Al, 6% [6]Al, and 4% [3]Al. During supercooling (T_m = 2283 K[11]), the amount of [4]Al increases more rapidly than in LAG, reaching 59% at 1770 K, while the fraction of [5]Al decreases. This trend matches that observed for [5]Al fractions in alkaline earth and rare earth modified aluminosilicates (melts and quenched glasses) as seen by ^{27}Al MAS NMR.[32–34] Models for temperatures below 1770 K are not available because the melt spontaneously crystallized at lower temperatures during X-ray measurements. From ^{27}Al MAS NMR measurements, YAG glass contained 68% [4]Al, 26% [5]Al, and 6% [6]Al, shown in Fig. 3(a) at T_g = 1159 K.[13]

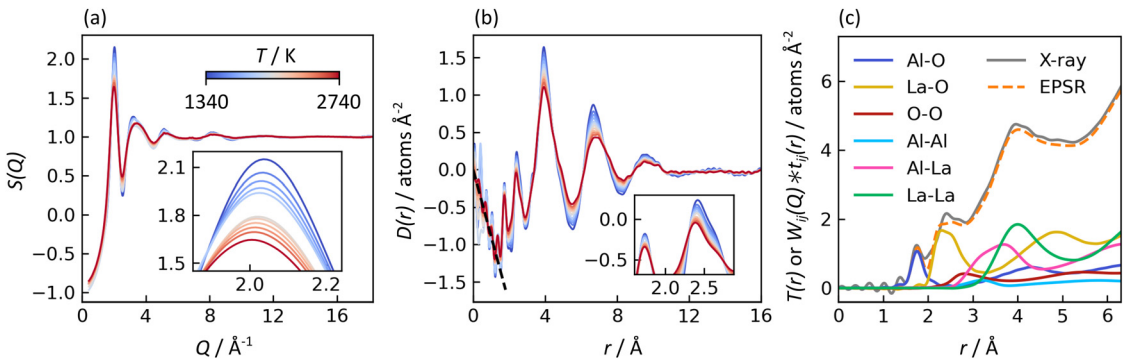

Fig. 1 High-energy X-ray diffraction of molten $La_3Al_5O_{12}$ (LAG). (a) Total structure factors, and (b) differential pair distribution functions (PDFs) over 1340–2740 K. The dashed black line in (b) represents the expected slope of $-4\pi\rho$ with ρ = 0.0712 atoms Å^{-3}. (c) Total PDF and X-ray weighted atomic partial pair correlations from EPSR at 2420 K.

Open Access Article. Published on 05 June 2025. Downloaded on 3/3/2026 10:40:12 AM.
This article is licensed under a Creative Commons Attribution-NonCommercial 3.0 Unported Licence.

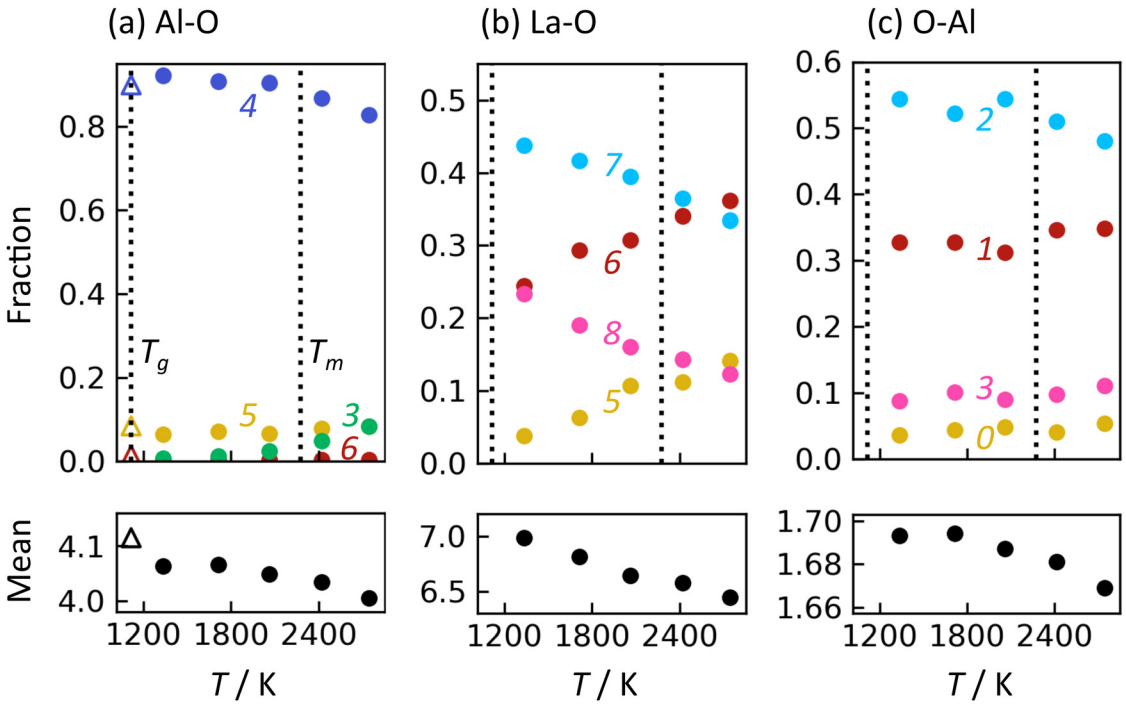

Fig. 2 Coordination number distributions and mean values in molten LAG for atom pairs (a) Al–O, (b) La–O, and (c) O–Al. For Al–O, room-temperature NMR measurements for LAG glass are shown at T_g with open triangle markers. Vertical dashed lines are T_g and T_m. Typical model uncertainties are ±0.08 for Al–O and La–O mean coordination numbers and ±0.03 for O–Al.

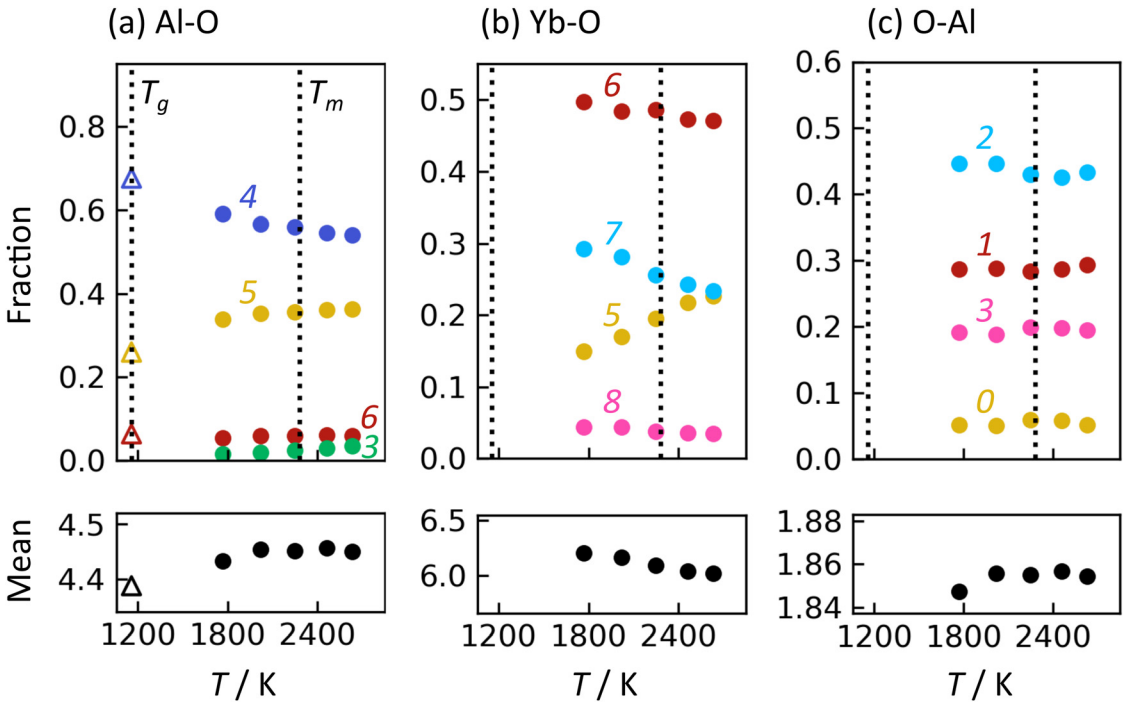

Fig. 3 Coordination number distributions and mean values in molten YbAG for atom pairs (a) Al–O, (b) Yb–O, and (c) O–Al. For Al–O, room-temperature NMR measurements for YAG glass are shown at T_g with open triangle markers. Vertical dashed lines are T_g and T_m. Typical model uncertainties are ±0.08 for Al–O and Yb–O mean coordination numbers and ±0.03 for O–Al.

Again, the glass values are in excellent agreement with the temperature trend from the EPSR models. Compared with Watanabe *et al.*,[15] the YAG glass here is 6% richer in $^{[4]}$Al and 5% poorer in $^{[6]}$Al. This discrepancy may be explained by the

Open Access Article. Published on 05 June 2025. Downloaded on 3/3/2026 10:40:12 AM.
This article is licensed under a Creative Commons Attribution-NonCommercial 3.0 Unported Licence.

somewhat lower magnetic field in the earlier study (11.7 T) and, consequently, significant overlap between the different Al resonances, contributing to a larger experimental uncertainty. Mean Al–O coordination decreases during cooling from 4.45 in the melt to 4.39 in the glass, counter to the trend observed for LAG (though both trends fall within the modeling uncertainty of ± 0.08).

Turning to the rare earth coordination environments, La–O distributions for LAG are shown in Fig. 2(b). Molten LAG at 2740 K contains roughly 35% each of LaO_6 and LaO_7 ($^{[6]}$La, $^{[7]}$La) and 15% each $^{[5]}$La and $^{[8]}$La. This broad distribution is consistent with the wide peak observed for the La–O X-ray partial pair correlation (Fig. 1(b) and (c)). Upon cooling, the fractions of $^{[7]}$La and $^{[8]}$La increase linearly while $^{[5]}$La and $^{[6]}$La decrease. Consequently, the mean La–O coordination number increases during cooling from 6.45 to 6.98. This is consistent with the shift of the La–O partial PDF's first peak to higher-*r* during cooling (Fig. S1(b), ESI†) and agrees well with the mean coordination of 7.0(1) previously reported for LAG glass.[35] Compared to LAG, the Yb–O distributions in YbAG are substantially different (Fig. 3(b)). Molten YbAG at 2630 K contains approximately 25% each of $^{[5]}$Yb and $^{[7]}$Yb, 45% $^{[6]}$Yb, and only a small amount of $^{[8]}$Yb. During cooling, $^{[7]}$Yb increases at the expense of $^{[5]}$Yb, and $^{[6]}$Yb and $^{[8]}$Yb increase only modestly. The resulting Yb–O mean coordination increases during cooling from 6.02 to 6.21, which matches a prior report of Y–O mean coordination of 6.1(1) for YAG glass.[35] Comparing LAG and YbAG melts, the minor fractions of $^{[5]}$La and $^{[8]}$Yb are consistent with expectations from cation–anion radius ratio rules, with La^{3+} being much larger and thus preferring higher coordination numbers than Yb^{3+}. The R–O mean coordination increases upon cooling in both melts, though with a stronger temperature dependence in LAG than in YbAG (0.38 per 1000 K, *vs.* 0.22).

The distributions of O–Al coordination are given in Fig. 2(c) for LAG and Fig. 3(c) for YbAG. Molten LAG is approximately 50% OAl_2 and 35% OAl, with ≤10% each of OAl_3 and oxygen bonded only with La. Molten YbAG contains roughly 45% OAl_2, 30% OAl, 20% OAl_3, and a minor fraction of oxygen bonded only with Yb. The substantially larger fraction of OAl_3 in YbAG leads to a larger mean O–Al coordination of 1.86 *vs.* ∼1.68 in LAG. Changes in O–Al coordination *vs.* temperature are subtle in both melts. Bond angle distributions for O–Al–O, O–R–O, and Al–O–Al are provided and discussed in the ESI.†

Having established the coordination environments for the extremes of glass formation in rare earth aluminum garnet compositions (LAG *vs.* YbAG/YAG), we next consider glasses of their compositional mixtures, $(La_{1-z}Y_z)_3Al_5O_{12}$. This pseudo-binary series provides insights to how the Al–O coordination changes as a function of mean rare earth size. ^{27}Al MAS NMR spectra for these glasses are shown in Fig. 4(a), with the Al–O coordination distributions from spectral peak fitting (see Fig. S2 for an example, ESI†) in Fig. 4(b). The spectra comprise broad, overlapping peaks as expected for glasses containing a diversity of local environments, and the YAG sample (z = 1) exhibits a small, sharp peak at 1 ppm chemical shift corresponding to crystalline AlO_6 in YAG[15] (<0.2%, excluded from the peak fitting). Qualitative confirmation of the different Al coordination environments, particularly for low fractions of $^{[6]}$Al in glasses with low z, is found by ^{27}Al 3QMAS NMR spectroscopy, an example of which is plotted in Fig. S2 (ESI†). As the mean rare earth size decreases (*i.e.*, increasing z), the amount of $^{[4]}$Al decreases nearly linearly from 90 to 68%, while $^{[5]}$Al and $^{[6]}$Al increase roughly linearly. The consistent trend *vs.* composition is notable, given that the glass becomes two-phase for z greater than *ca.* 0.71.[36–38]

Additionally, as shown by the tabulated fitting results (Table S2, ESI†) the smaller rare earth size also appears to cause an increase in the ^{27}Al quadrupolar coupling constant (C_Q) for both $^{[4]}$Al and $^{[5]}$Al, reflecting a distinct change in the symmetry of these environments. Arnaud *et al.*[39] demonstrated that ionic field strength of charge-balancing cations can significantly affect the magnitude of C_Q for AlO_4 tetrahedra in aluminoborosilicate glasses, and thus the increasing C_Q for $^{[4]}$Al in these rare earth aluminate glasses reflects the increasing concentration of higher field strength Y^{3+} (relative to La^{3+}). A systematic increase in the Gaussian distribution of the

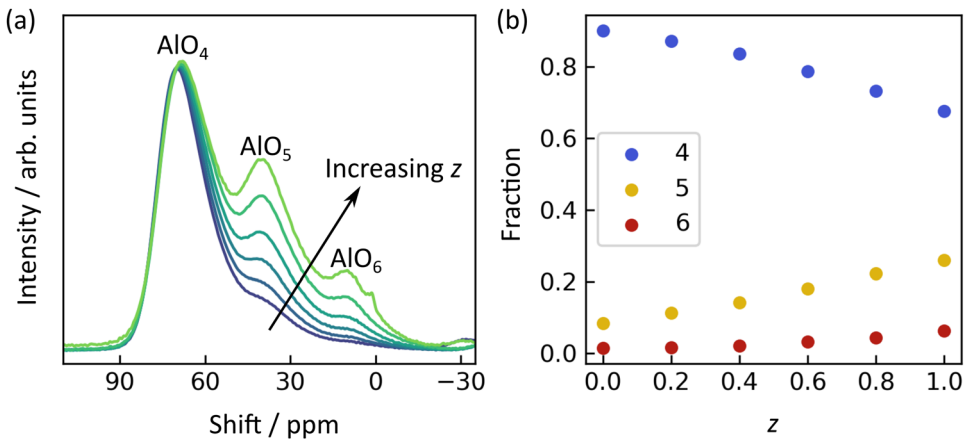

Fig. 4 (a) ^{27}Al MAS NMR spectra of $(La_{1-z}Y_z)_3Al_5O_{12}$ glasses, for z = 0, 0.2, 0.4, 0.6, 0.8, and 1.0. (b) Coordination number distributions for Al–O, calculated from spectral peak fitting; uncertainty due to peak overlap is ±1%.

Open Access Article. Published on 05 June 2025. Downloaded on 3/3/2026 10:40:12 AM.
This article is licensed under a Creative Commons Attribution-NonCommercial 3.0 Unported Licence.

isotropic chemical shift for $^{[4]}$Al is also evident, possibly also related to these changes in rare earth ion field strength.

3.2. Aluminum–oxygen network

Key structural aspects affecting glass formation include the connectivity and linkedness among Al–O polyhedra. Connectivity refers to the number of polyhedra neighboring a given polyhedron, conventionally represented by the Q^n distribution for tetrahedral networks (n = 0 to 4), while linkedness refers to the number of oxygen shared between a given pair of polyhedra (L = 0 to 3, corresponding to isolated, corner-, edge-, and face-sharing).[40]

Fig. 5 shows the frequency of different polyhedra connections, sorted by their linkedness, for molten LAG at 2420 K and YbAG at 2460 K. In LAG, Al–O polyhedra are linked by 91% corner-sharing (CS) and 9% edge-sharing (ES), with negligible connectivity among $^{[5]}$Al and $^{[6]}$Al due to their low populations. In YbAG, there is 80% CS and 19% ES overall, with most of the edge-sharing involving the $^{[5]}$Al and $^{[6]}$Al polyhedra that are more prevalent than in LAG. Face-sharing (FS) is negligible in both melts. Similar linkedness has been reported for molten Al_2O_3: 83% CS and 16% ES, with most of the ES occurring with one or two $^{[5]}$Al or $^{[6]}$Al units.[31] Although Al_2O_3 cannot be melt quenched to form a glass, its ability to supercool by 500 K indicates that it is not far from the threshold of glass formation.[41] The comparatively larger CS fraction in LAG (91%) and smaller fraction in YbAG (80%) are consistent with glass formation only attainable in LAG, though nearly crystal-free glass can be quenched from YbAG.[13] When considering only $^{[4]}$Al–$^{[4]}$Al connections, the three melts have similar CS fractions: 95% in LAG, 94% in YbAG, and 96% in Al_2O_3.[31]

3.2.1. Network connectivity definitions. Before further discussion of the network structure, it is important to define which structural units are considered network formers and which are modifiers. While this binary classification is broadly useful in glass science, its application here is tricky because Al_2O_3 is an intermediate. More specifically, Sun[42] organized various oxides as network formers, intermediates, or modifiers based on their metal–oxygen bond dissociation energies: tetrahedral $^{[4]}$Al was grouped with the network formers, while $^{[6]}$Al was considered an intermediate. This analytical approach is similar to that of Hudon and Baker,[43] who point out that amphoteric cations such as Al^{3+} create bonds with greater covalent character when 4-coordinate than when 6-coordinate. Due to the greater ionicity of the latter, $^{[6]}$Al is typically considered a modifier. Its propensity for close packing and edge-sharing also lead to crystal nucleation. The case of $^{[5]}$Al is less clear,[44] and many analyses of aluminate glasses do not consider it as part of the network, for example during calculations of connectivity. To explore how $^{[5]}$Al might be participating in the network, we will look at how connectivity analyses differ when considering the network as comprising solely $^{[4]}$Al, *vs.* both $^{[4]}$Al and $^{[5]}$Al.

To do so, we define a metric of connectivity, K^n (the capital Greek letter kappa), that is distinct but analogous to the commonly used Q^n distribution. The conventional Q^n analysis makes three assumptions about the glass network: entirely tetrahedral, all corner-sharing, and no triply bonded oxygen. None of these assumptions hold for the aluminate networks in this study, so an alternative connectivity definition is necessary to compare LAG and YbAG. For clarity, we define nonbridging oxygen (NBO), bridging oxygen (BO), and triply bonded oxygen (TBO) as oxygen that are bonded to 1, 2, or 3 network-forming cations, respectively. It is worth noting a few implications of these definitions. First, if a structural unit is not considered part of the network, such as $^{[6]}$Al, then those Al^{3+} cations are ignored for connectivity calculations. Second, the classification of a given oxygen may be different depending on the network definition. For example, an oxygen shared between one $^{[4]}$Al and one $^{[5]}$Al would be a NBO if the network comprises only $^{[4]}$Al, but it would be a BO if the network comprises $^{[4]}$Al and $^{[5]}$Al. Third, some oxygen bonded to Al will be excluded from the connectivity analysis, for example if they are only bonding in $^{[6]}$Al units.

In the Q^n convention, the value of n for a given network-forming tetrahedron is interchangeably (and equivalently) defined as the number of neighboring network-forming tetrahedra or the number of its BO. For K^n, n is similarly defined to be the number of neighboring network-forming polyhedra, but this is no longer necessarily equivalent to the number of BO. To calculate K^n, we first consider a network unit without edge-shares or TBO: in this case, n is equal to the number of BO since each BO connects to one neighboring network unit. If two corner-sharing links are replaced with one edge-share, the number of neighboring network units decreases by one. If a BO is replaced with a TBO, the number of neighboring network units increases by one. (Or, equivalently, each TBO represents two neighboring units.) Thus, the resulting formula for K^n of a given network polyhedron is:

$$n = \mathrm{BO} - \mathrm{ES} + (2 \times \mathrm{TBO}) \quad (1)$$

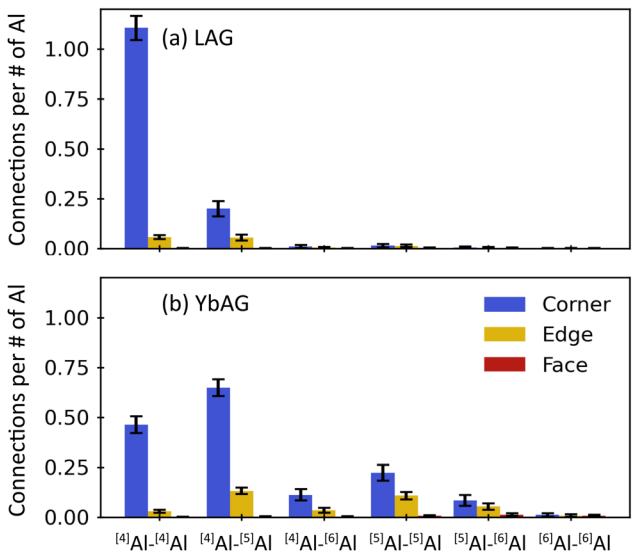

Fig. 5 Connectivity and linkedness between Al–O polyhedra, distinguished by polyhedra coordination 4, 5, or 6. (a) Molten LAG at 2420 K and (b) YbAG at 2460 K. Error bars represent the standard deviations across simulation configurations.

Open Access Article. Published on 05 June 2025. Downloaded on 3/3/2026 10:40:12 AM.
This article is licensed under a Creative Commons Attribution-NonCommercial 3.0 Unported Licence.

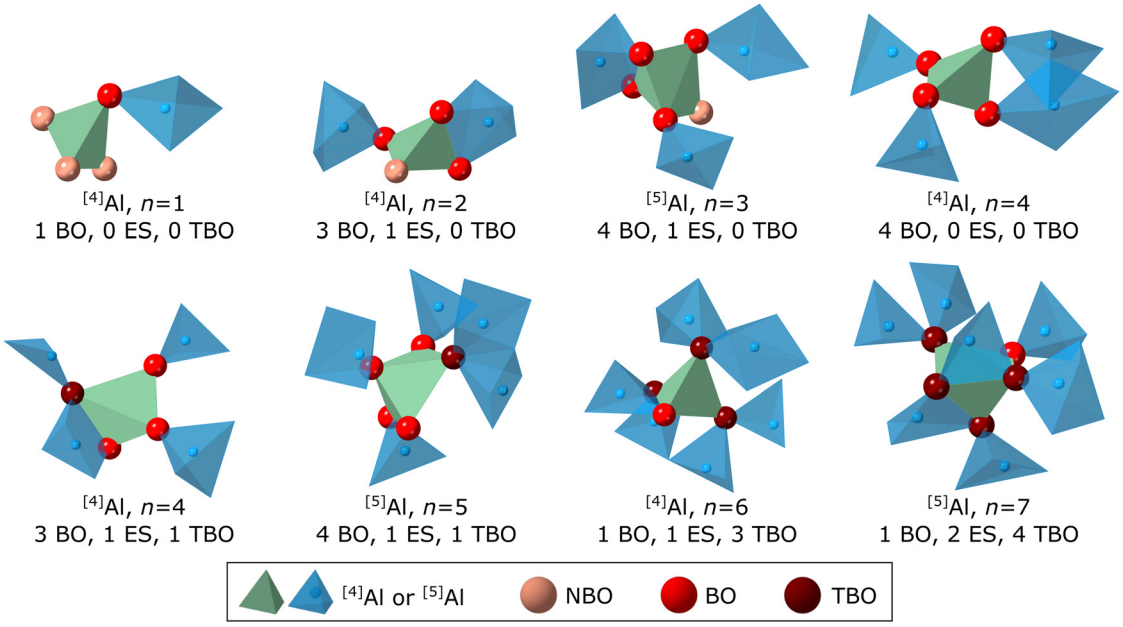

Fig. 6 Atomic arrangements in molten YbAG at 2460 K selected to illustrate the calculation of K^n for network connectivity. For each of the 8 examples, the Al–O polyhedron being analyzed is shown in opaque green, its coordinated oxygen are shown with spheres (NBO, BO, and TBO), and all the neighboring network-forming polyhedra are shown in translucent blue. The oxygen beyond the first coordination shell and all Yb are not shown, for clarity.

For illustration, Fig. 6 shows atomic arrangements in a network comprising $^{[4]}$Al and $^{[5]}$Al units that correspond to different K^n. These range, for example, from n = 1 (1 BO, 0 ES, 0 TBO) to n = 7 (1 BO, 2 ES, 4 TBO). The value of n in the K^n analysis preserves the same meaning regarding connectivity as it does for Q^n analysis of tetrahedral CS networks without TBO: n is the number of neighboring network units. That aside, interpretation of K^n is different in several ways compared to Q^n. The definition in eqn (1) allows both $^{[4]}$Al and $^{[5]}$Al units to exist in a wide range of K^n states, from n = 0 for an isolated polyhedron up to either n = 8 for $^{[4]}$Al or n = 10 for $^{[5]}$Al if all its oxygen were TBO and it had no ES. Also, a given K^n does not correspond uniquely to one atomic arrangement. For example, a $^{[4]}$Al unit that is K^4 can correspond to a tetrahedron with 4 BO and no ES, or to a tetrahedron with 3 BO, 1 TBO, and 1 ES (Fig. 6, n = 4 examples). These two different arrangements each result in 4 neighboring network units.

As n increases, NBO are less common and TBO become more prevalent, as shown in Fig. 6. The presence of TBO also correlates with the presence of ES. Of the network-forming $^{[4]}$Al and $^{[5]}$Al units that participate in at least 1 ES, 79–85% have at least 1 TBO. This correlation is consistent in both LAG and YbAG across all temperatures that were modeled.

3.2.2. A network of $^{[4]}$Al. We will now use the K^n analysis to compare connectivity in LAG and YbAG, first considering the network to comprise only $^{[4]}$Al tetrahedra. This network definition follows the standard models for binary rare earth aluminates, such as those described by Watanabe *et al.*[15] or Cormier,[44] which we will briefly review here for context. By analyzing the network in relation to the ratio [O]/[Al], these models have been applied to alkali, alkaline earth, and rare earth aluminates. When [O]/[Al] = 2, the alkali, alkaline earth, or rare earth content can perfectly charge-compensate the −1 charge per AlO_4 tetrahedra, making possible a continuous Q^4 network of corner-sharing AlO_4, at least from a charge balance perspective. Experimental studies on alkaline earth aluminate glasses with [O]/[Al] = 2, corresponding to $50Al_2O_3$–50MO (M = Ca, Sr, Ba), have shown that essentially all Al are present as AlO_4.[17–19] When additional MO is added, [O]/[Al] > 2 and the network structure must change to accommodate the excess modifier. This typically happens by depolymerization of the network: replacing a bridging oxygen (BO) with two non-bridging oxygen (NBO), thus shifting Q^4 units to Q^3, while all Al remain $^{[4]}$Al. In the case of insufficient MO, [O]/[Al] < 2, the structure again must make accommodations to achieve local charge balance. These accommodations include formation of $^{[5]}$Al and $^{[6]}$Al, conventionally considered as having a modifier-type role, and possibly the formation of oxygen triclusters (TCO), defined as an oxygen that is connected to three tetrahedra.[45,46] (Note: while considering the network to be only $^{[4]}$Al in this study, TCO are equivalent to TBO since $^{[5]}$Al are not considered part of the network.) Experimental measurements have clearly shown higher-coordinated Al, while the occurrence of TCO remains disputed in the glass literature due to the tremendous difficulty in measuring them experimentally.[44,47,48]

This model works well for the alkaline earth systems,[17–19] but greater structural complexity is present in the Al–O networks of rare earth aluminates. Even at the [O]/[Al] = 2 composition, $75Al_2O_3$–$25R_2O_3$, not all Al are present as $^{[4]}$Al. In binary aluminate glasses with 27% La_2O_3 or 26% Y_2O_3, $^{[5]}$Al is present at 13% and 28%, respectively.[15] Watanabe *et al.*[15] proposed that the formation of higher-coordinated Al in these systems occurs because of the

 This journal is © the Owner Societies 2025

Open Access Article. Published on 05 June 2025. Downloaded on 3/3/2026 10:40:12 AM.
This article is licensed under a Creative Commons Attribution-NonCommercial 3.0 Unported Licence.

high charge of the 3+ rare earth cations, combined with their relatively small sizes (*i.e.*, high cation field strength, CFS). The CFS is much higher for La (0.5 $Å^{-2}$) and Y (0.58 $Å^{-2}$) than for the alkaline earths (0.26–0.36 $Å^{-2}$), so they strongly attract the electron density from surrounding oxygen. Preferably, each R^{3+} would be surrounded with three AlO_4 tetrahedra. This is marginally possible with the larger rare earths like La^{3+}, but for the smaller rare earths, corner-sharing tetrahedra cannot pack sufficiently close and so instead higher-coordinated Al are formed. This packing problem is consistent with the difference that we observe in mean La–O and Yb–O coordination, with the former being larger due to the greater size of La^{3+}. Our findings are generally consistent with Watanabe *et al.*'s explanation, with a few minor exceptions: our EPSR models show predominantly CS among $^{[5]}$Al and $^{[6]}$Al in YbAG (Fig. 5(b)), whereas Watanabe suggested these polyhedra would be linked mostly by ES, and our models indicate a possibility of TCO, discussed below.

We turn now to the network structure observed in this study for LAG and YbAG melts and glasses, which have [O]/[Al] = 2.4. Because these compositions are in the excess modifier regime, the presence of $^{[5]}$Al and $^{[6]}$Al indicate that other structural accommodations are being made for charge balance. The EPSR models exhibit an array of these accommodations, including higher-coordinated Al (Fig. 2(a) and 3(a)), mixtures of CS and ES, $^{[4]}$Al network depolymerization, and perhaps the creation of TCO. The fractions of CS and ES in the $^{[4]}$Al network are shown in Fig. 7(a). Both molten LAG (circle markers) and YbAG (triangle markers) contain ∼6% ES arrangements *ca.* 2600 K, but during cooling these are replaced by CS. The temperature trend of linkedness is nearly linear and ends with essentially 100% CS at T_g. The temperature dependence of the ES-to-CS shift may be slightly weaker in YbAG than in LAG, though the magnitude of this difference falls within the models' uncertainties.

The K^n distributions for $^{[4]}$Al tetrahedra in LAG and YbAG melts are given in Fig. 7(b). In LAG, the distribution is predominantly K^2 and K^3, with a mean connectivity of $\bar{n}$ = 2.67. In YbAG, the K^n distribution shape is similar but is shifted downward by 1 unit, with $\bar{n}$ = 1.79. Thus, the $^{[4]}$Al network is much more disconnected in YbAG and ∼14% of $^{[4]}$Al are K^0, *i.e.*, completely isolated from other $^{[4]}$Al tetrahedra. Fractions of BO, NBO, and TCO for the oxygen in the $^{[4]}$Al networks are shown in Fig. 7(c). In LAG at 2420 K, networked oxygen comprise 39% BO, 57% NBO, and 4% TCO. In YbAG, there are 24% BO, 74% NBO, and 2% TCO. The larger NBO fraction in YbAG is consistent with the more fragmented $^{[4]}$Al network compared to LAG. During cooling, both melts replace ∼4% of the NBO with BO. The percentages for TCO are quite small and may be an artifact of EPSR's tendency to produce highly disordered models. The occurrence of TCO in LAG does not change significantly when using a larger Al–O cutoff distance of 2.45 Å. Still, their marginal presence in the models should be interpreted with caution.

The oxygen fractions shown in Fig. 7(c) were calculated by normalizing to the number of networked oxygen. The total oxygen is equal to the sum of networked oxygen and free oxygen (FO). For this network definition, FO are any oxygen bonded only as part of $^{[5]}$Al, $^{[6]}$Al, and/or La–O polyhedra. Free oxygen constitute 6–11% of the total oxygen in LAG and 29–32% of the total oxygen in YbAG. The larger FO percentage in YbAG is consistent with its larger fractions of $^{[5]}$Al and $^{[6]}$Al.

3.2.3. A network of $^{[4]}$Al and $^{[5]}$Al. Next, we repeat the same network analysis but define the network as comprising both $^{[4]}$Al and $^{[5]}$Al. Conventionally, $^{[5]}$Al have often been considered as modifiers to the tetrahedral network.[44] However, the highly disconnected $^{[4]}$Al network of molten YbAG motivates a discussion of the role that $^{[5]}$Al plays in glass formation. Specifically, the comparison of ^{27}Al NMR for YAG glass (Fig. 4(b)) with EPSR extrapolations of supercooled YbAG (Fig. 3(a)) indicate that the two materials likely have very similar structures. Since YAG does form glass, and the YbAG $^{[4]}$Al network is seemingly unsuitable for glass formation (14% isolated units and 29% K^1), it is plausible that $^{[5]}$Al contributes something to network formation.

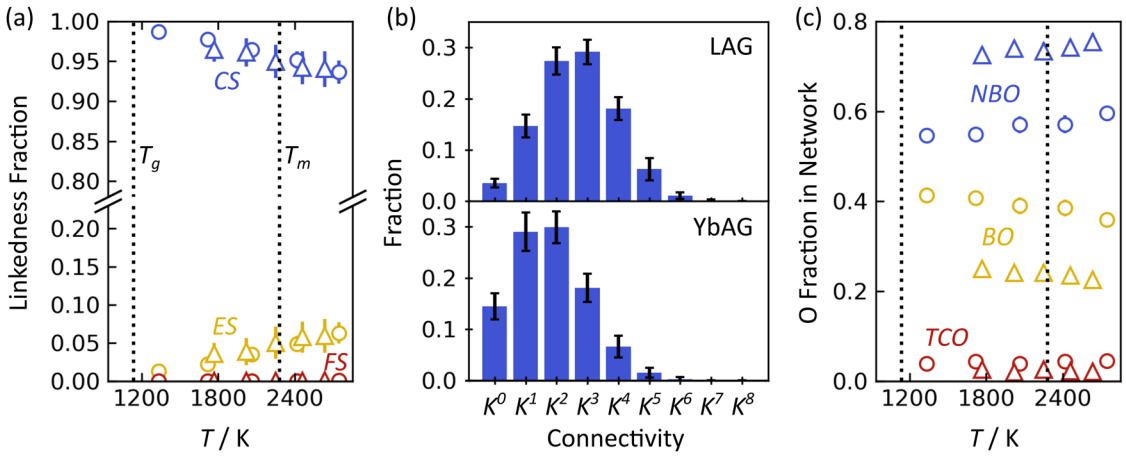

Fig. 7 Structure of the $^{[4]}$Al network. (a) Linkedness fractions for corner-sharing (CS), edge-sharing (ES), and face-sharing (FS) arrangements. LAG is shown with circle markers; YbAG with triangle markers. (b) K^n distributions for LAG at 2420 K and YbAG at 2460 K. (c) Fractions of NBO, BO, and tricluster oxygen (TCO). Error bars represent the standard deviations across simulation configurations.

Open Access Article. Published on 05 June 2025. Downloaded on 3/3/2026 10:40:12 AM.
This article is licensed under a Creative Commons Attribution-NonCommercial 3.0 Unported Licence.

To explore this idea, the network was reanalyzed while including all [4]Al and [5]Al polyhedra in the network. The results are shown in Fig. 8, which can be directly compared with the analysis for the network of only [4]Al in Fig. 7. When [5]Al are included in the network analysis, the linkedness fractions include more ES, shown in Fig. 8(a), as was alluded to with Fig. 5. For YbAG, in particular, ES constitutes 16% in the network at high temperatures and decreases only slightly upon cooling. In LAG, ES decreases from 10% to 4% during cooling.

As shown in Fig. 8(b), the K^n distributions for LAG and YbAG are more similar to each other when [5]Al are considered part of the network. LAG, containing mostly [4]Al, is upshifted only slightly as compared with Fig. 7(b). However, YbAG exhibits a large upshift compared to Fig. 7(b) because the [5]Al units are now counted in the network. The [4]Al units in YbAG are now predominantly K^3 and K^4 as expected from the bulk composition, and the amount of K^0 [4]Al has dropped from 14% in Fig. 7(b) to 2% in Fig. 8(b). The connectivity distribution for [5]Al units is situated at higher n values than the [4]Al distribution, as expected. Mean connectivity is $\bar{n}$ = 3.02 in LAG and $\bar{n}$ = 3.45 in YbAG. If analyzed with the conventional Q^n assumptions, the garnet bulk composition of [O]/[Al] = 2.4 would be expected to have $\bar{n}$ = 3.2. The earlier network definition of only [4]Al units (Fig. 7) resulted in a large deviation between the structural $\bar{n}$ and what would typically be expected for this [O]/[Al], whereas including [5]Al in the network (Fig. 8) restores the link between the bulk chemistry and mean connectivity of the network. During cooling, the K^n distributions shift upward slightly due to the decrease in ES and slight increase in BO, leading to an increase of $\bar{n}$ by ~0.15.

The fractions of oxygen in the network are given in Fig. 8(c). Again, the results for LAG are only slightly different than in Fig. 7(c): the fraction of BO has increased slightly at the expense of NBO, consistent with the inclusion of more Al–O polyhedra in the network analysis. For YbAG, this shift is much larger, and the NBO and BO fractions now match closely those in LAG. The TBO fraction in YbAG is nearly double that of LAG, 11% *vs.* 6%. Now that [5]Al is included in the network, FO correspond to oxygen bonding only as part of [6]Al and/or La–O polyhedra. Free oxygen constitute only 4–8% of the total oxygen in LAG and 7–8% in YbAG.

These comparisons of Fig. 7 and 8 highlight how the results of network analyses can differ remarkably depending on what structural units are included in the network definition. There is considerable ambiguity in deciding on a network definition for the rare earth aluminates because the role of [5]Al is unclear. A limitation of the K^n distribution calculations is that they require [5]Al to be either "in" or "out," even if they do not fit neatly into the categories of network former or modifier. From the perspective of a [4]Al network, the lower glass forming ability of YbAG as compared to LAG correlates with a much more disconnected network and larger NBO population. From the perspective of a network comprising [4]Al and [5]Al, YbAG's lower glass forming ability correlates with more ES, which is not replaced with CS during cooling, and a larger fraction of TBO.

The lack of [6]Al is favorable to glass formation. The Al_2O_3–Yb_2O_3 and Al_2O_3–Y_2O_3 systems stabilize the garnet crystal structure, which contains [6]Al, whereas the Al_2O_3–La_2O_3 system does not stabilize the garnet structure and its melt contains little [6]Al, likely preventing a packing where the garnet structure could form. Moving across the rare earth series in decreasing order of trivalent cation size, the garnet phase becomes stable for Eu (0.947 Å for 6-coordinate[16]) and smaller rare earths, which is a similar trend to the glass forming ability of garnet composition melts, for which vitrification stops at Y (0.9 Å).[13]

4. Conclusion

The melt structures of $R_3Al_5O_{12}$ (R = La or Yb) have been analyzed and compared to better understand their differences in glass forming ability. Structural models obtained by EPSR

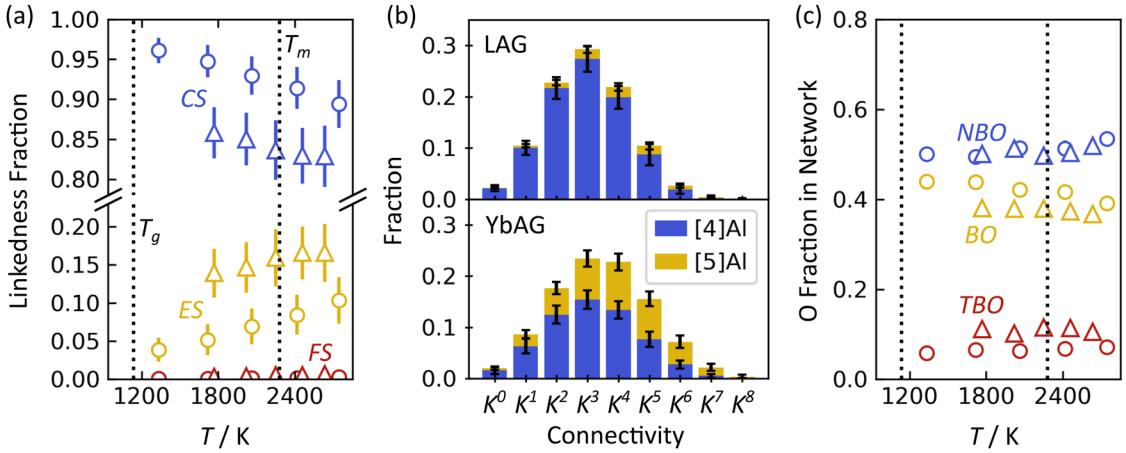

Fig. 8 Structure of the [4]Al and [5]Al network. (a) Linkedness fractions for CS, ES, and FS arrangements. LAG is shown with circle markers; YbAG with triangle markers. (b) K^n distributions for LAG at 2420 K and YbAG at 2460 K. (c) Fractions of NBO, BO, and TBO. Error bars represent the standard deviations across simulation configurations.

Open Access Article. Published on 05 June 2025. Downloaded on 3/3/2026 10:40:12 AM.
This article is licensed under a Creative Commons Attribution-NonCommercial 3.0 Unported Licence.

are in excellent agreement with high-energy X-ray diffraction data, and levitation melting provided access to deeply supercooled melts and vitrification of LAG. During cooling, changes in the mean coordination numbers are slight for Al–O, ±0.1, and moderate for R–O, +0.5 for La–O and +0.2 for Yb–O, which are driven by an increase in 7- and 8-coordinate R–O polyhedra at the expense of 5- and 6-coordinate. The Al–O coordination number distributions, when extrapolated from the supercooled melts, are in close agreement with ^{27}Al MAS NMR measurements of the room-temperature glasses. Changes in Al–O coordination number distributions trend roughly linearly with the mean size of the rare earth cations, based on NMR measurements of ternary composition glasses.

In the melts, linkedness in the Al–O networks is mostly corner-sharing, except with considerable (>20%) edge-sharing among $^{[5]}$Al and $^{[6]}$Al units in YbAG. Network connectivity was compared using a newly defined metric, K^n, which adapts the commonly used Q^n distribution to account for the effects of $^{[5]}$Al units, edge-sharing, and triply bonded oxygen. When defining the glass network as only $^{[4]}$Al tetrahedra, molten LAG and YbAG exhibit similar polyhedra linkedness, with 6% edge-sharing that converts to corner-sharing upon cooling before reaching the glass transition. The $^{[4]}$Al network in LAG comprises mostly K^2 and K^3 units, while YbAG exhibits a highly disconnected network of mostly K^1 and K^2. If $^{[5]}$Al are also included in the network analysis, YbAG instead contains predominantly K^3 and K^4 like LAG, but edge-sharing increases to 16%. During cooling, network connectivity increases slightly due to the decrease in edge-sharing and a slight increase of bridging oxygen.

The lower glass forming ability of YbAG compared to LAG correlates with larger fractions of $^{[5]}$Al and $^{[6]}$Al, lower connectivity among $^{[4]}$Al units, increased edge-sharing involving $^{[5]}$Al units, and a higher fraction of triply bonded oxygen.

Author contributions

Stephen K. Wilke: conceptualization (equal), formal analysis (lead), investigation (equal), methodology (lead), supervision (lead), writing – original draft (lead), writing – review & editing (equal). Chris J. Benmore: investigation (equal), writing – review & editing (equal). Randall E. Youngman: formal analysis (supporting), investigation (equal), writing – original draft (supporting), writing – review & editing (equal). Benjamin J. A. Moulton: formal analysis (supporting), methodology (supporting), writing – review & editing (equal). Abdulrahman Al-Rubkhi: formal analysis (supporting), methodology (supporting). Richard Weber: conceptualization (equal), funding acquisition (lead), investigation (equal), supervision (supporting), writing – review & editing (equal).

Data availability

X-ray structure factors for molten LAG and ^{27}Al NMR spectra for glasses are available in the ESI.† Other supporting data are available from the corresponding author upon reasonable request.

Conflicts of interest

There are no conflicts of interest to declare.

Acknowledgements

This work was supported by the National Aeronautics and Space Administration (NASA) through grant 80NSSC18K0059. BJAM appreciates support from Alfred University and Dr. Katherine Faber. This research was performed on APS beam time award (DOI: https://doi.org/10.46936/APS-183682/60011543) from the Advanced Photon Source, a U.S. Department of Energy (DOE) Office of Science user facility operated for the DOE Office of Science by Argonne National Laboratory under Contract No. DE-AC02-06CH11357.

References

1 J. W. Drazin and R. S. Hay, Refractive index and lattice parameter prediction for garnets (A3B2C3X12), *J. Am. Ceram. Soc.*, 2023, **106**, 3853–3866.
2 M. C. Wilding, in *Ceramic and Glass Materials*, ed. J. F. Shackelford and R. H. Doremus, Springer US, Boston, MA, 2008, pp. 49–70.
3 F. D. Patel, E. C. Honea, J. Speth, S. A. Payne, R. Hutcheson and R. Equall, Laser demonstration of Yb3Al5O12 (YbAG) and materials properties of highly doped Yb:YAG, *IEEE J. Quantum Electron.*, 2001, **37**, 135–144.
4 J. Ueda and S. Tanabe, Review of luminescent properties of Ce3+ doped garnet phosphors: New insight into the effect of crystal and electronic structure, *Opt. Mater.:X*, 2019, **1**, 100018.
5 W. Jin, W. Yin, S. Yu, M. Tang, T. Xu, B. Kang and H. Huang, Microwave dielectric properties of pure YAG transparent ceramics, *Mater. Lett.*, 2016, **173**, 47–49.
6 E. A. Mironov and O. V. Palashov, Faraday isolator based on TSAG crystal for high power lasers, *Opt. Express*, 2014, **22**, 23226–23230.
7 Y. Huang, K. Zhao, S. Dong, K. Lü, J. Jiang, L. Deng, W. Chen and X. Cao, Thermal cycling and steam corrosion behavior of Yb3Al5O12-based multilayered environmental barrier coatings for SiC_f/SiC, *J. Am. Ceram. Soc.*, 2025, **108**, 1–14.
8 B. S. Hulbert, J. L. Stokes, M. J. Presby and G. Costa, Comparison of laser-based and solid-state syntheses of ytterbium aluminum garnet Yb3Al5O12, *J. Am. Ceram. Soc.*, 2025, 1–9.
9 D. Massiot, F. Taulelle and J. P. Coutures, Structural Diagnostic of High Temperature Liquid Phases by 27Al NMR, *Le J. Phys., Colloq.*, 1990, **51**, 425–431.
10 J. K. R. Weber, J. J. Felten, B. Cho and P. C. Nordine, Glass fibres of pure and erbium- or neodymium-doped yttria-alumina compositions, *Nature*, 1998, **393**, 769–771.

Open Access Article. Published on 05 June 2025. Downloaded on 3/3/2026 10:40:12 AM.
This article is licensed under a Creative Commons Attribution-NonCommercial 3.0 Unported Licence.

11 P. Wu and A. D. Pelton, Coupled thermodynamic-phase diagram assessment of the rare earth oxide-aluminium oxide binary systems, *J. Alloys Compd.*, 1992, **179**, 259–287.
12 M. Pianassola, K. Anderson, C. Agca, C. J. Benmore, J. W. McMurray, J. C. Neuefeind, C. Melcher and M. Zhuravleva, In Situ High-Temperature Structural Analysis of High-Entropy Rare-Earth Sesquioxides, *Chem. Mater.*, 2023, **35**, 1116–1124.
13 Y. Watanabe, A. Masuno and H. Inoue, Glass formation of rare earth aluminates by containerless processing, *J. Non-Cryst. Solids*, 2012, **358**, 3563–3566.
14 R. Weber, S. Hampton, P. C. Nordine, T. Key and R. Scheunemann, Er3+ fluorescence in rare-earth aluminate glass, *J. Appl. Phys.*, 2005, **98**, 1–26.
15 Y. Watanabe, A. Masuno, H. Inoue, Y. Yanaba and K. Kato, Influence of modifier cations on the local environment of aluminum in La2O3–Al2O3 and Y2O3–Al2O3 binary glasses, *Phys. Chem. Chem. Phys.*, 2020, **22**, 19592–19599.
16 R. D. Shannon, Revised effective ionic radii and systematic studies of interatomic distances in halides and chalcogenides, *Acta Crystallogr., Sect. A*, 1976, **32**, 751–767.
17 P. F. McMillan, W. T. Petuskey, B. Coté, D. Massiot, C. Landron and J.-P. Coutures, A structural investigation of CaO-Al2O3 glasses via 27Al MAS-NMR, *J. Non-Cryst. Solids*, 1996, **195**, 261–271.
18 M. Licheron, V. Montouillout, F. Millot and D. R. Neuville, Raman and 27Al NMR structure investigations of aluminate glasses: $(1 - x)Al2O3 - xMO$, with M = Ca, Sr, Ba and $0.5 < x < 0.75$), *J. Non-Cryst. Solids*, 2011, **357**, 2796–2801.
19 D. R. Neuville, L. Cormier and D. Massiot, Al coordination and speciation in calcium aluminosilicate glasses: Effects of composition determined by 27Al MQ-MAS NMR and Raman spectroscopy, *Chem. Geol.*, 2006, **229**, 173–185.
20 J. K. R. Weber, C. J. Benmore, G. Jennings, M. C. Wilding and J. B. Parise, Instrumentation for fast in-situ X-ray structure measurements on non-equilibrium liquids, *Nucl. Instrum. Methods Phys. Res.*, 2010, **624**, 728–730.
21 J. K. R. Weber, C. J. Benmore, L. B. Skinner, J. Neuefeind, S. K. Tumber, G. Jennings, L. J. Santodonato, D. Jin, J. Du and J. B. Parise, Measurements of liquid and glass structures using aerodynamic levitation and in-situ high energy x-ray and neutron scattering, *J. Non-Cryst. Solids*, 2014, **383**, 49–51.
22 S. K. Wilke, A. Al-Rubkhi, C. J. Benmore, J. Neuefeind, C. Koyama, T. Ishikawa, R. Shimonishi and R. Weber, Structure of molten ytterbium aluminum garnet, *J. Chem. Phys.*, 2025, **162**, 124501.
23 D. A. Keen, A comparison of various commonly used correlation functions for describing total scattering, *J. Appl. Crystallogr.*, 2001, **34**, 172–177.
24 C. J. Benmore, A Review of High-Energy X-Ray Diffraction from Glasses and Liquids, *ISRN Mater. Sci.*, 2012, **2012**, 1–19.
25 S. K. Wilke, O. L. G. Alderman, C. J. Benmore, J. Neuefeind and R. Weber, Octahedral oxide glass network in ambient pressure neodymium titanate, *Sci. Rep.*, 2022, **12**, 8258.
26 A. K. Soper, Empirical potential Monte Carlo simulation of fluid structure, *Chem. Phys.*, 1996, **202**, 295–306.
27 M. Suta, W. Urland, C. Daul and C. Wickleder, Photoluminescence properties of Yb^{2+} ions doped in the perovskites CsCaX3 and CsSrX3 (X = Cl, Br, and I) – a comparative study, *Phys. Chem. Chem. Phys.*, 2016, **18**, 13196–13208.
28 M. Chaika, O. Vovk, G. Mancardi, R. Tomala and W. Strek, Dynamics of Yb2+ to Yb3+ ion valence transformations in Yb:YAG ceramics used for high-power lasers, *Opt. Mater.*, 2020, **101**, 109774.
29 D. Massiot, F. Fayon, M. Capron, I. King, S. Le Calvé, B. Alonso, J.-O. Durand, B. Bujoli, Z. Gan and G. Hoatson, Modelling one- and two-dimensional solid-state NMR spectra, *Magn. Reson. Chem.*, 2002, **40**, 70–76.
30 J.-P. Amoureux, C. Fernandez and S. Steuernagel, Z Filtering in MQMAS NMR, *J. Magn. Reson., Ser. A*, 1996, **123**, 116–118.
31 L. B. Skinner, A. C. Barnes, P. S. Salmon, L. Hennet, H. E. Fischer, C. J. Benmore, S. Kohara, J. K. R. Weber, A. Bytchkov, M. C. Wilding, J. B. Parise, T. O. Farmer, I. Pozdnyakova, S. K. Tumber and K. Ohara, Joint diffraction and modeling approach to the structure of liquid alumina, *Phys. Rev. B*, 2013, **87**, 024201.
32 P. Florian, N. Sadiki, D. Massiot and J. P. Coutures, 27Al NMR study of the structure of lanthanum- And yttrium-based aluminosilicate glasses and melts, *J. Phys. Chem. B*, 2007, **111**, 9747–9757.
33 J. F. Stebbins, E. V. Dubinsky, K. Kanehashi and K. E. Kelsey, Temperature effects on non-bridging oxygen and aluminum coordination number in calcium aluminosilicate glasses and melts, *Geochim. Cosmochim. Acta*, 2008, **72**, 910–925.
34 C. Le Losq, D. R. Neuville, P. Florian, G. S. Henderson and D. Massiot, The role of Al3+ on rheology and structural changes in sodium silicate and aluminosilicate glasses and melts, *Geochim. Cosmochim. Acta*, 2014, **126**, 495–517.
35 R. Weber, C. J. Benmore, J. Siewenie, J. Urquidi and T. S. Key, Structure and bonding in single- and two-phase alumina-based glasses, *Phys. Chem. Chem. Phys.*, 2004, **6**, 2480.
36 J. A. Tangeman, B. L. Phillips, P. C. Nordine and J. K. R. Weber, Thermodynamics and structure of single- and two-phase yttria-alumina glasses, *J. Phys. Chem. B*, 2004, **108**, 10663–10671.
37 L. B. Skinner, A. C. Barnes, P. S. Salmon and W. A. Crichton, Phase separation, crystallization and polyamorphism in the Y2O3-Al2O3 system, *J. Phys.: Condens. Matter*, 2008, **20**, 205103.
38 J. K. R. Weber, J. G. Abadie, A. D. Hixson, P. C. Nordine and G. A. Jerman, Glass formation and polyamorphism in rare-earth oxide-aluminium oxide compositions, *J. Am. Ceram. Soc.*, 2000, **83**, 1868–1872.
39 A. Quintas, T. Charpentier, O. Majérus, D. Caurant, J. L. Dussossoy and P. Vermaut, NMR Study of a Rare-Earth Aluminoborosilicate Glass with Varying CaO-to-Na2O Ratio, *Appl. Magn. Reson.*, 2007, **32**, 613–634.
40 F. Liebau, *Structural Chemistry of Silicates*, Springer, Berlin, Heidelberg, 1985.
41 C. Shi, O. L. G. Alderman, D. Berman, J. Du, J. Neuefeind, A. Tamalonis, J. K. R. Weber, J. You and C. J. Benmore,

 This journal is © the Owner Societies 2025

Open Access Article. Published on 05 June 2025. Downloaded on 3/3/2026 10:40:12 AM.
This article is licensed under a Creative Commons Attribution-NonCommercial 3.0 Unported Licence.

The Structure of Amorphous and Deeply Supercooled Liquid Alumina, *Front. Mater.*, 2019, **6**, 1–15.
42 K. Sun, Fundamental Condition of Glass Formation, *J. Am. Ceram. Soc.*, 1947, **30**, 277–281.
43 P. Hudon and D. R. Baker, The nature of phase separation in binary oxide melts and glasses. I. Silicate systems, *J. Non-Cryst. Solids*, 2002, **303**, 299–345.
44 L. Cormier, *Encyclopedia of Materials: Technical Ceramics and Glasses*, Elsevier, 2021, pp. 496–518.
45 E. D. Lacy, Aluminium in glasses and in melts, *Phys. Chem. Glasses*, 1963, **4**, 234–238.
46 J. F. Stebbins and Z. Xu, NMR evidence for excess non-bridging oxygen in an aluminosilicate glass, *Nature*, 1997, **390**, 60–62.
47 I. Daniel, P. F. McMillan, P. Gillet and B. T. Poe, Raman spectroscopic study of structural changes in calcium aluminate (CaAl2O4) glass at high pressure and high temperature, *Chem. Geol.*, 1996, **128**, 5–15.
48 D. Iuga, C. Morais, Z. Gan, D. R. Neuville, L. Cormier and D. Massiot, NMR heteronuclear correlation between quadrupolar nuclei in solids, *J. Am. Chem. Soc.*, 2005, **127**, 11540–11541.